Journal of Applied Physics

Pressure driven phase transitions in honeycomb $Fe_4Nb_2O_9$: A possible re-entrant multiferroic behavior

Cite as: J. Appl. Phys. **131**, 084101 (2022); https://doi.org/10.1063/5.0083331
Submitted: 24 December 2021 • Accepted: 03 February 2022 • Published Online: 24 February 2022

Mrinmay Sahu, Bishnupada Ghosh, Rajesh Jana, et al.

Journal of Applied Physics ARTICLE scitation.org/journal/jap

Pressure driven phase transitions in honeycomb $Fe_4Nb_2O_9$: A possible re-entrant multiferroic behavior

Cite as: J. Appl. Phys. **131**, 084101 (2022); doi: 10.1063/5.0083331
Submitted: 24 December 2021 · Accepted: 3 February 2022 ·
Published Online: 24 February 2022

Mrinmay Sahu,[1] Bishnupada Ghosh,[1] Rajesh Jana,[2,a)] Jinguang Cheng,[2] and Goutam Dev Mukherjee[1,b)]

AFFILIATIONS

[1]National Centre for High Pressure Studies, Department of Physical Sciences, Indian Institute of Science Education and Research Kolkata, Mohanpur Campus, Mohanpur 741246, Nadia, West Bengal, India
[2]Beijing National Laboratory for Condensed Matter Physics and Institute of Physics, Chinese Academy of Sciences, Beijing 100190, China

[a)]**Present Address:** Solid State Physics Division, Bhabha Atomic Research Centre, Mumbai 400085, India.
[b)]**Author to whom correspondence should be addressed:** goutamdev@iiserkol.ac.in

ABSTRACT

A detailed high-pressure investigation is carried out on $Fe_4Nb_2O_9$ using angle resolved x-ray diffraction and Raman spectroscopy measurements. We find a structural transition from the ambient trigonal phase to a monoclinic phase above 8.8 GPa. The structural transition is assumed to be driven by a large distortion of $Nb–O_6$ octahedra as seen from x-ray diffraction analysis and a large pressure dependence of an $Nb–O_6$ octahedra breathing Raman mode. Anomalous behavior of Raman modes and an increase in the phonon lifetime at the phase transition pressure indicate a possible change in the magnetic property of the sample above 8.8 GPa. A decrease in the diffusive scattering rate of a low-frequency electronic contribution contradicts the results of a decrease in the intensity of a high-frequency electronic response and excludes the phenomenon of an insulator to metal transition. On the contrary, the enhancement of the intensity of the Raman modes up to about 8.8 GPa indicates a large change in ferroelectric polarization of the sample, indicating a possible pressure induced re-entrant multiferroic behavior in $Fe_4Nb_2O_9$.

I. INTRODUCTION

Recent developments in information technology are linked to various devices, such as multistage storage memory devices, sensors, spintronic devices, etc., which utilize electric and magnetic properties of materials. The strongly correlated systems, which exhibit mutual coupling of multiple order parameters, have attracted widespread research interest due to their innovative technological applications.[1] Multiferroic materials hold great application possibilities for the development of electronic devices because of the coexistence of ferroelectric and magnetic orders and their outstanding mutual coupling.[1–4] This can lead to significant magneto-electric (ME) coupling in multiferroic materials, in which the magnetic information can be controlled by an electric field or the electric polarization by an external magnetic field.[5,6] There are spin-driven (type II) multiferroics in which specific magnetic ordering is responsible for the inversion symmetry breaking. CuO, $GdFeO_3$, $TbMnO_3$, etc., belong to type II multiferroics, and they exhibit ME coupling.[7–9] Apart from a type II multiferroic system, a new class of $A_4B_2O_9$ (where A = Fe, Co, Mn and B = Nb, Ta) compounds crystallizing in centrosymmetric crystal structures exhibit a novel linear-ME (LME) effect.[1,10–13]

Some of the above types of materials exhibit a collinear antiferromagnetic structure at the ground state.[10,14–17] The crystallographic structure of $A_4B_2O_9$ is derived from magnetoelectric corundum-type Cr_2O_3, which belongs to the centrosymmetric layered trigonal structure with the *P*-3*c*1 space group.[18] The layered trigonal crystallographic structures are generally formed by two different types of honeycomb layers stacked alternately along the *c*-axis. Recently, $Mn_4Nb_2O_9$, $Co_4Nb_2O_9$, and $Fe_4Nb_2O_9$ are reported to belong to the LME class.[11,14,19,20]

Temperature dependent magnetic susceptibility $\chi(T)$ and neutron diffraction measurements on honeycomb $Fe_4Nb_2O_9$ (FNO) show the antiferromagnetic transition at $T_N = 94$ K, with a strong magnetic anisotropy suggesting in-plane antiferromagnetic exchange iterations and out of plane ferromagnetic exchange interactions between Fe atoms along the *c*-axis.[14,15,21] Dielectric permittivity measurements on the same material show two anomalies at 94 and 80 K due to magnetic transition and trigonal *P*-3*c*1 to monoclinic *C*2/*c* structural phase transition, respectively.[14,15,22,23]

Recently, it is reported that in LME $Co_4Nb_2O_9$, the lattice distortion causes the change in bond strength leading to an anisotropic magneto-dielectric coupling phenomenon.[24] Hence, it is important to understand the effect of strain on the physical properties of FNO, as it also belongs to the LME class. FNO contains $3d^6$ Fe^{2+} magnetic cations having a high spin state (S = 2), consistent with the O^{2-} and Nb^{5+} oxidation state. The Jahn–Teller (JT) distortion of $Fe^{2+}O_6$ octahedra removes the degeneracy of t_{2g} orbitals and consequently tends to localize electrons via a local lattice distortion.[25] Carrier delocalization can be possible by lifting the JT distortion of the octahedra. In strongly correlated systems, charge delocalization is identified from the electron–phonon scattering rate that can be obtained from low-frequency electronic (LFE) contributions and the softening of the high-frequency electronic (HFE) peak from Raman spectroscopy measurements.[26–30] The reduction of octahedral distortion (hence the JT coupling) can be possible by applying the external pressure on the system. Therefore, studying the physical behavior of FNO at high pressures will be very interesting, which is lacking as far as the knowledge of the authors.

In this work, we have carried out high-pressure x-ray diffraction (XRD) and Raman scattering experiments on polycrystalline FNO. Detailed high-pressure XRD data analysis allows us to explain the change in bond lengths formed by the heavy ions in the honeycomb layers and determine a structural phase transition from an ambient trigonal *P*-3*c*1 to a monoclinic *C*2/*c* phase at about 8.8–9.3 GPa. The FNO unit cell is found to be more compressible along the *c*-axis in comparison with the *ab*-plane, indicating competition between two types of exchange interactions at high pressures. Our pressure-dependent Raman-scattering data show a change in the slope and a minimum in the FWHM of selected Raman modes around 8.8 GPa. The anomalous behavior of Raman modes in combination with analysis of the structural data indicates a magnetic transition along with a possible change in lattice electrical polarization in the monoclinic phase at high pressures.

II. EXPERIMENTAL

Powder FNO samples were synthesized through a conventional solid-state synthesis route as described in the literature.[14] We have carried out high-pressure XRD and Raman spectroscopy measurements using a piston-cylinder type diamond anvil cell (DAC) from EasyLab Co. (UK) having a 300 μm culet. Polycrystalline FNO samples were crushed into a very fine powder and loaded inside a hole of a 120 μm diameter drilled in a pre-indented stainless-steel gasket. The indented thickness of the gasket was about 50 μm. A methanol–ethanol (4 : 1) mixture was added as a pressure transmitting medium (PTM). The pressure-dependent XRD measurements at room temperature were carried out at the XPRESS beamline in an ELETTRA synchrotron source in Trieste, Italy. The wavelength of the monochromatic x-ray beam was 0.4957 Å. The incident high energy x-ray radiation was collimated

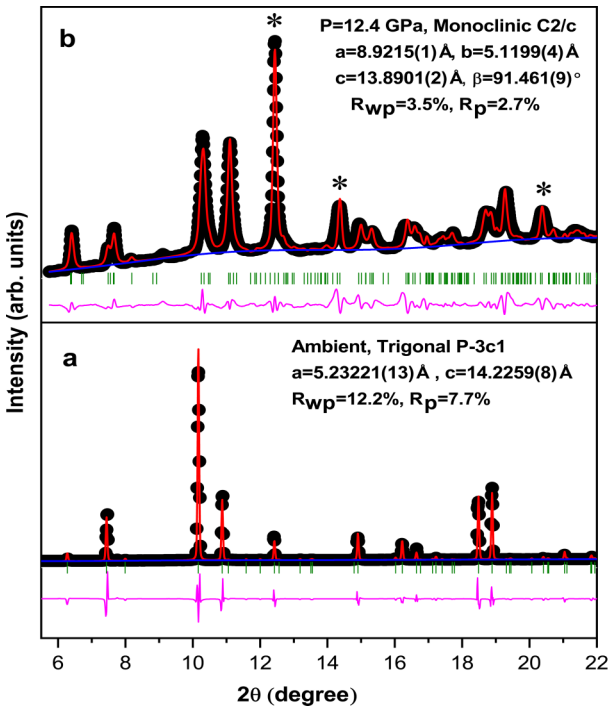

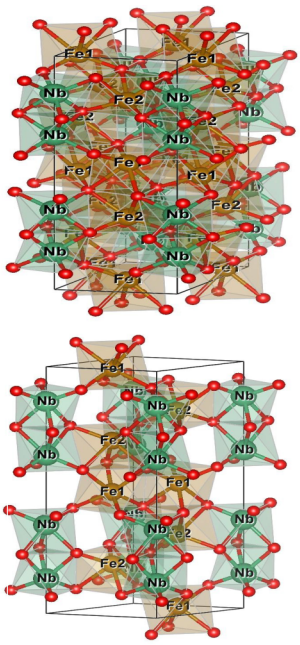

FIG. 1. Rietveld refined XRD patterns of polycrystalline $Fe_4Nb_2O_9$ at (a) ambient pressure (trigonal phase in space group *P*-3*c*1) and (b) 12.4 GPa after transition (monoclinic phase in space group *C*2/*c*). The bold black circle indicates observed data points, the fitted values are represented by the red line over the data points, and the pink line below denotes the difference between the observed and fitted intensities. The pressure marker silver peaks are indicated by "*." The right side of the XRD pattern shows the arrangements of the metal–oxygen polyhedra with the lower one belonging to the trigonal phase and the upper one to the monoclinic phase.

to about 30 μm. The diffraction patterns were recorded using a MAR-345 image plate detector, placed normal to the incident beam. A minute amount of fine silver powder was added along with the sample during loading of DAC. Equation of state of silver was used for the determination of pressure values *in situ*.[31] The sample to the detector distance was calibrated using LaB_6. Diffracted patterns were integrated to 2θ vs intensity profile using FIT2D software.[32] The XRD patterns were indexed using CRYSFIRE,[33] and for the refinement of the unit cell parameter, we used CHECKCELL.[34] Lebail and Rietveld refinements of all the XRD patterns were carried out using GSAS software.[35]

Pressure-dependent Raman spectroscopy measurements were performed using the confocal micro-Raman system (Monovista from S&I GmbH). Raman signals were collected in the backscattering geometry. A few ruby chips (approximate sizes of 3–5 μm) were added along with the sample during loading the DAC for pressure calibration using the ruby fluorescence technique.[36] The sample was excited using a Cobalt-Samba diode pump 532 nm laser source. Raman signals were collected using an infinitely corrected 20× objective lens having a large working distance and a grating of 1500 rulings/mm with a spectral resolution of about 1.2 cm^{-1}. For detailed Raman analysis, we have collected the Raman spectra from 100 cm^{-1} to get rid of any effect of the edge filter used to remove the Rayleigh line, which was standardized from the Raman spectra of Si (Fig. S1 in the supplementary material).

III. RESULTS AND DISCUSSIONS

We have collected the XRD patterns of polycrystalline FNO at different pressures up to 30 GPa. At ambient conditions, all the diffraction peaks can be well indexed to the trigonal unit cell with the *P*-3*c*1 symmetry. The Rietveld refinement of the ambient pattern is carried out using the initial atom positions obtained from Jana *et al.*[14] and shown in Fig. 1(a). The calculated lattice parameters from the best fit are a = 5.232 21(13) Å, c = 14.2259(8) Å, and corresponding unit cell volume V = 338(6) $Å^3$. These are quite close to the literature values.[14] In Fig. S2 of the supplementary material, we have plotted pressure dependence of XRD patterns at selected pressure points. The XRD patterns of the FNO sample show no significant changes up to 8.8 GPa. Changes in the diffraction patterns are observed with the appearance of splitting of certain Bragg peaks around 9.3 GPa as shown in Fig. S2(a) of the supplementary material. With a further increase in pressure, more Bragg peaks start splitting and they are found to be well resolved by about 15.3 GPa [Fig. S2(b) in the supplementary material]. We indexed the XRD pattern at 12.4 GPa, which returned a monoclinic structure with lattice parameters, $a = 8.9215(1)$, $b = 5.1199(4)$, $c = 13.8901(2)$ Å, and $\beta = 91.461(9)^\circ$, and corresponding unit cell volume V = 634.26(3) $Å^3$. For a better understanding of the crystal structure at high pressures, we have performed group–subgroup analysis using Bilbao Crystallographic Server tools. The symmetry-related maximal subgroup of *P*-3*c*1 is the subgroup *C*2/*c* having space group number 15. The XRD pattern at 12.4 GPa is best matched to the above lattice parameters in the C2/c space group. The new structure is very much similar to the antiferromagnetic monoclinic phase obtained by Jana *et al.* below 85 K.[14] The Rietveld refinements of the monoclinic phase are carried out by calculating the atom position parameters using group–subgroup analysis using the software Powder Cell.[37,38] The best Rietveld fit of the XRD pattern at 12.4 GPa is shown in Fig. 1(b) using new atom positions, which are given in Table I. We used the same monoclinic structure to index the XRD patterns from 9.3 GPa, which gave a good match. Therefore, we observe a structural transition at about 9.3 GPa from the trigonal to

TABLE I. Atomic coordinates and isotropic displacement parameters ($Å^2$) of $Fe_4Nb_2O_9$ refined from XRD data at 12.4 GPa in space group No. 15 (*C*2/*c*, *Z* = 4). Lattice parameters are *a* = 8.9215(1) Å, *b* = 5.1199(4) Å, *c* = 13.8901(2) Å, β = 91.461(9)°, and *V* = 634.26(3) $Å^3$. The goodness of fit parameters are R_{wp} = 3.51% and R_p = 2.74%.

Atom	Site	*x*	*y*	*z*	U_eq
Nb	8*f*	0.000 000	0.000 000	0.160(3)	0.009 5(4)
Fe1	8*f*	0.166(5)	0.500 0	0.199 6(7)	0.005 32(2)
Fe2	8*f*	0.166(6)	0.500 0	0.967 8(8)	0.009 5(1)
$O1_1$	8*f*	0.012 6(8)	0.671 9(7)	0.088 9(8)	0.009 7(13)
$O1_2$	8*f*	0.157 67(5)	0.183 04(5)	0.088 9(8)	0.009 7(13)
$O1_3$	8*f*	0.329 6(4)	0.644 9(9)	0.088 9(8)	0.009 7(13)
$O2_1$	4*e*	0.000 000	0.287 000	0.250 000	0.014(3)
$O2_2$	8*f*	0.356(5)	0.356(5)	0.250 000	0.014 00(3)

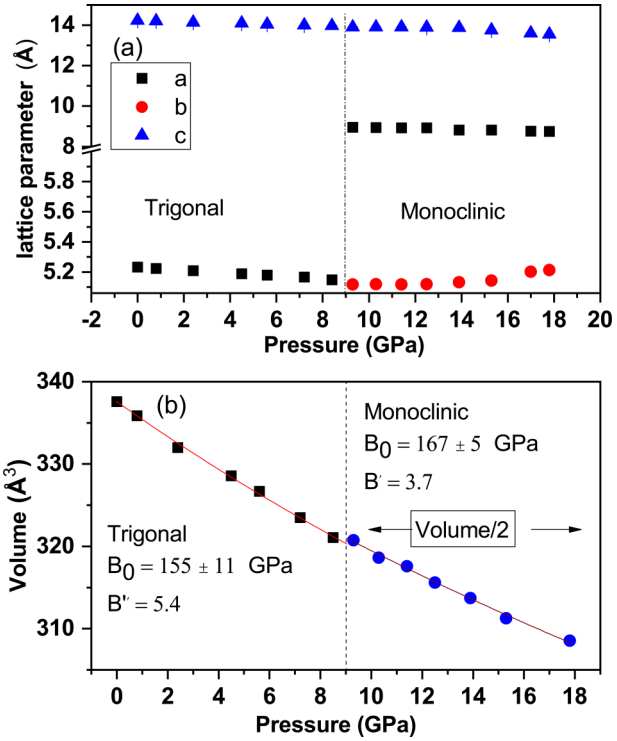

FIG. 2. Pressure evolution of (a) unit cell lattice parameters and (b) unit cell volume of polycrystalline $Fe_4Nb_2O_9$. The lines passing through the volume is the Birch–Murnaghan EOS fit to the volume data.

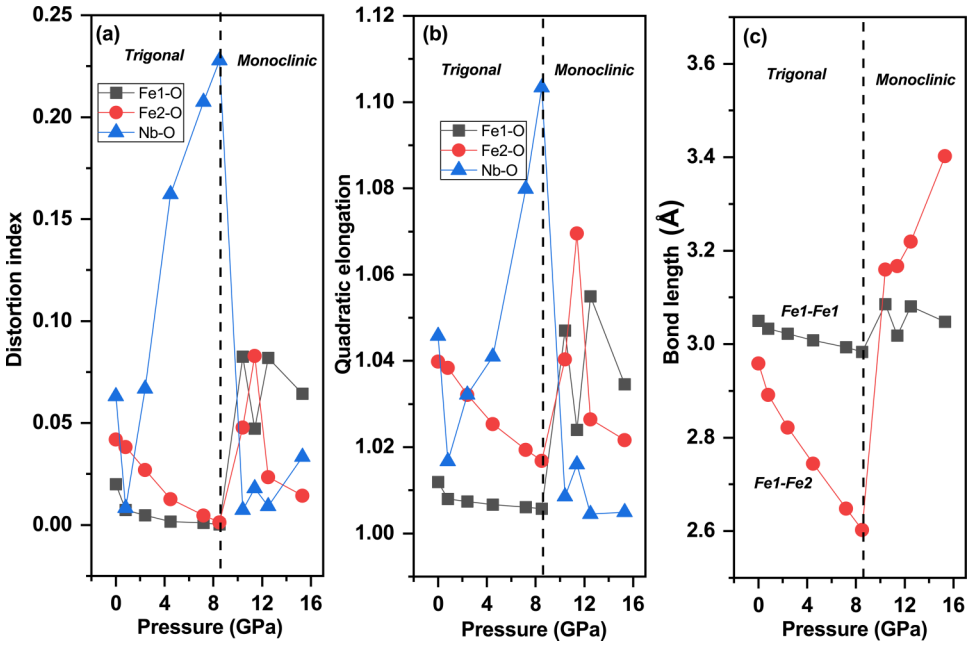

FIG. 3. (a) Distortion index and (b) quadratic elongation of metal–oxygen octahedra at different pressures. (c) Distance between Fe1–Fe2 atoms along the *c*-axis and Fe1–Fe1 atoms in the *ab*-plane at various pressures The vertical dashed line marks the pressure value at the trigonal to monoclinic phase transition.

the monoclinic phase. No changes are observed upon a further increase in pressure except the broadening of peaks.

The pressure evolution of lattice parameters is shown in Fig. 2(a) for both the phases. The *c*-axis does not show any drastic change across the phase transition pressure. However, the *a*-axis shows a jump at the transition pressure. The *b*-axis, in the case of the monoclinic phase, shows a slight upturn at high pressures. The unit cell volume obtained after refinement of each XRD pattern at all pressure points (in both the phases) fitted to the 3rd order BM-EOS function[39] and is shown in Fig. 2(b),

$$P(V) = \frac{3B_0}{2}\left[\left(\frac{V_0}{V}\right)^{7/3} - \left(\frac{V_0}{V}\right)^{5/3}\right] \times \left\{1 + \frac{3}{4}(B' - 4)\left[\left(\frac{V_0}{V}\right)^{2/3} - 1\right]\right\}, \quad (1)$$

where B_0 and B' are the bulk modulus and the first-order pressure derivative of the bulk modulus, respectively. P is the pressure, and V_0 is the ambient unit cell volume. The obtained EOS parameters are as follows: for the trigonal phase, $B_0 = 155 \pm 11$ GPa, $B' = 5.4$, and for the monoclinic phase, $B_0 = 167 \pm 5$ GPa, $B' = 3.7$. Our results indicate a decrease in compressibility with the structural transition.

It is interesting to see the unit cell arrangement of FNO. The trigonal phase consists of layers of metal–oxygen polyhedra along the *c*-axis. There are two layers formed by edge shared NbO_6 and $Fe2O_6$ octahedra separated by a single layer formed by edge sharing $Fe1O_6$ octahedra along the *c*-axis. With the application of pressure, the distortion index and the quadratic elongation of both the $Fe1{-}O_6$ and $Fe2{-}O_6$ octahedra decrease up to about 8.8 GPa and then suddenly jumps in the monoclinic phase. In contrast, both the distortion index and the quadratic elongation of $Nb{-}O_6$ octahedra reach their respective maximum values at the phase boundary of trigonal to monoclinic phases as shown in Figs. 3(a) and 3(b). Since there is a minimal change in volume across the structural transition (from 160.5 Å^3 at 8.8 GPa to 160.2 Å^3 at 9.3 GPa), the large distortion of $Nb{-}O_6$ octahedra may be driving the structural transition. The effect of a small volume change can be seen from the starting of splitting of certain Bragg peaks at 9.3 GPa, which continue until they are well resolved at 12.4 GPa. Another important part is that the ambient trigonal phase undergoes a magnetic transition to an antiferromagnetic state below 95 K,[1,14,15] in which the spins of Fe atoms are aligned ferromagnetically along the *c*-axis and antiferromagnetically in the *ab*-plane. Therefore, we monitored the changes in the separation of Fe1 − Fe1 atoms and Fe1–Fe2 atoms in the *ab*-plane and along the *c*-axis, respectively, in Fig. 3(c). We find that for both the cases, the separation decreases and the relative change for Fe1–Fe2 atoms along the *c*-axis is more compared to that for Fe1–Fe1 in the *ab*-plane. However, from this information alone, it is not possible to suggest changes in the magnetic behavior of FNO at about 8.8 GPa, as the net magnetic structure depends on the competition among several exchange interactions present in the solid.

For complementary investigation of FNO under pressure, we have carried out the Raman spectroscopy studies on the same. We shall first discuss the ambient Raman spectrum as shown in Fig. 4(a). The spectrum shows seven Raman peaks with a broad continuum, the intensity of which increases below 200 cm^{-1} and shows a broad peak in the range of 500–900 cm^{-1}. FNO crystallizes in the trigonal crystal structure with the space group *P*-3*c*1, having two formula units, and it has 30 atoms per primitive cell, which leads to 57 optical phonon and 3 acoustic phonon modes in the

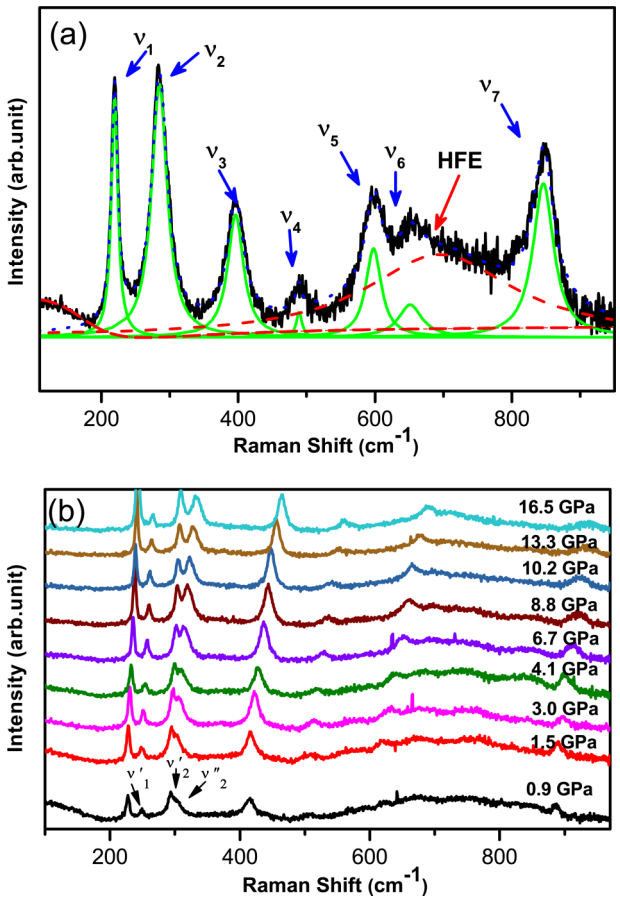

FIG. 4. (a) The deconvolution of the ambient Raman spectrum along with its fit using the Eq. (2) (b) Raman spectra at selected pressure points. The new mode ν_1' and the split modes ν_2' and ν_2'' are marked.

Brillouin zone center.[40] Group theory predicts the following representation of all the vibrational modes in the zone center boundary: $6A_{1g} + 9A_{1u} + 6A_{2g} + 9A_{2u} + 12E_g + 18E_u$, in which all the A_{1g} and E_g vibrational modes are Raman active. Hence, there are 18 Raman active modes, but experimentally, we see only seven well defined modes. The well defined modes are labeled as $\nu_1 = 220\,\mathrm{cm}^{-1}$, $\nu_2 = 282\,\mathrm{cm}^{-1}$, $\nu_3 = 396\,\mathrm{cm}^{-1}$, $\nu_4 = 490\,\mathrm{cm}^{-1}$, $\nu_5 = 598\,\mathrm{cm}^{-1}$, $\nu_6 = 650\,\mathrm{cm}^{-1}$, and $\nu_7 = 850\,\mathrm{cm}^{-1}$. The ambient Raman spectrum of FNO is in good agreement with the reported spectra.[40] Following the literature, we assign ν_1, ν_2, and ν_5 to E_g modes and ν_3 and ν_7 as A_{1g} modes.[40,41] $\nu_3 = 396\,\mathrm{cm}^{-1}$ and $\nu_7 = 850\,\mathrm{cm}^{-1}$ are internal vibrational modes due to the stretching and breathing motions of Nb–O_6 octahedra, respectively.[41–43]

Next, we shall discuss the general observation of the pressure evolution of Raman modes, which are shown in Fig. 4(b). All the mode frequencies show a blue shift with increasing pressure as expected due to compression in volume. We observe that a new mode (ν_1') appears at a low pressure of about 0.9 GPa. This new mode becomes stronger with pressure. The mode ν_2 splits into two modes, ν_2' and ν_2''. With increase in pressure, the intensity of ν_2'' increases and becomes comparable to ν_2'. The splitting of the two low frequency modes at such a low pressure value without any structural transition is quite an interesting phenomenon. Possibly, there are some microscopic changes in the FNO unit cell, which can give rise to a local ordering effect resulting in the appearance of new peaks in the Raman spectrum. It can be noted here that a sudden decrease in Nb–O_6 octahedra distortion is observed from a room pressure value to 0.8 GPa (see Fig. 3), beyond which it increases sharply. In fact, as we discussed earlier, during the pressure induced structural transition, only a large change in the distortion of Nb–O_6 octahedra is observed. Therefore, in all possibility, the emergence and splitting of Raman modes are probably driven by a change in the local structural order due to the change in Nb–O_6 octahedral distortion. Since we do not find any increase in the number of Raman modes above the phase transition pressure to the monoclinic structure, we believe that the Nb–O_6 octahedra distortion induces the formation of a local monoclinic structure at the microscopic level. This is probably missed by the XRD measurements since it gives an average crystal structure. Above 9.3 GPa, the monoclinic phase attains a significant proportion to be detected by the XRD. The low frequency diffusive continuum becomes gradually flat with pressure and almost disappears above about 6.7 GPa [Fig. 4(b)]. Similarly, the broad continuum in the range of 500–900 cm^{-1} decreases above about 8.8 GPa. The strong pressure dependence shows this feature to be intrinsic to the sample in origin. Similar features are seen in other strongly correlated oxide insulators showing magnetic anomalies.[26–29,44,45]

Further detailed analysis of the pressure evolution of Raman spectra is carried out by multiplying each spectrum using the Bose–Einstein thermal factor. The Raman-scattering response of FNO in the 100–950 cm^{-1} frequency range can be well fitted [as shown in Fig. 4(a)] with the spectral response[29]

$$S(\nu) = S_{ph}(\nu) + S_{el}(\nu), \tag{2}$$

where

$$S_{ph}(\nu) = [1 + n(\nu)] \sum_{1}^{n} \frac{A_i \nu \Gamma_i}{(\nu^2 - \nu_i^2)^2 + \nu^2 \Gamma_i^2} \tag{3}$$

represents n phonon peaks ($n = 7$ for ambient and $n = 9$ above 0.9 GPa) with associated peak frequency ν_i, amplitude A_i, and linewidth Γ_i,

$$S_{el}(\nu) = [1 + n(\nu)] \left[\frac{A\nu/\tau}{\nu^2 + 1/\tau^2} + \frac{A_{el}\nu\Gamma_{el}}{(\nu^2 - \nu_{el}^2)^2 + \nu^2\Gamma_{el}^2} \right], \tag{4}$$

where the first right hand side term represents a low-frequency electronic (LFE) response due to diffusive hopping of the carriers with a scattering rate $1/\tau$ and the second term represents a high-frequency electronic (HFE) contribution near $\nu_{el} \sim 550{-}900\,\mathrm{cm}^{-1}$. The term $[1 + n(\nu)]$ represents the Bose–Einstein thermal factor. Our data fit extremely well to the above equations [Fig. 4(a)].

Figure 5(a) shows the pressure evolution of significant Raman modes. All the modes show linear behavior with respect to pressure

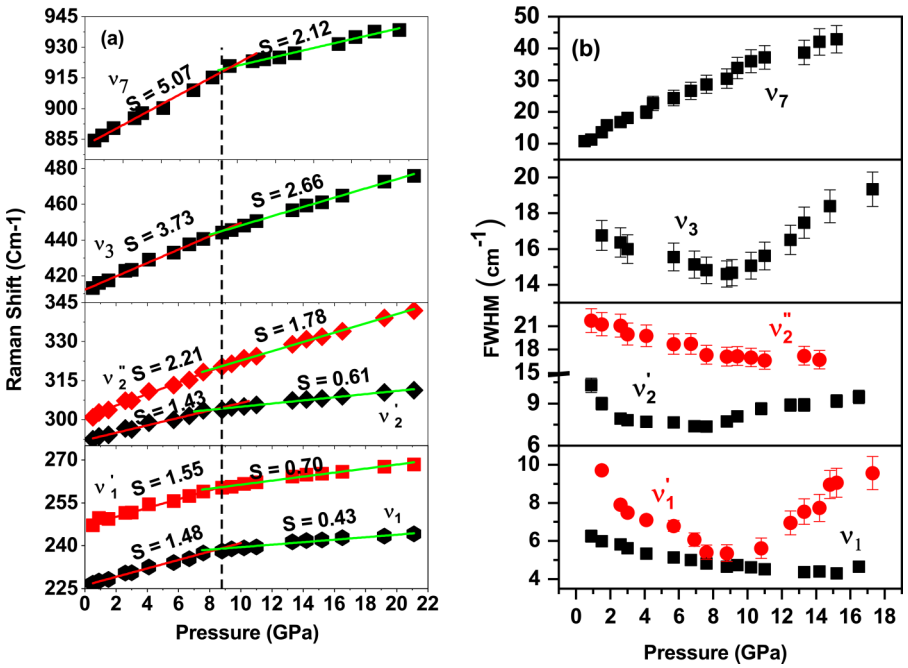

FIG. 5. (a) Pressure evolution of significant Raman modes showing changes in the slope in their linear in pressure behavior at 8.8 GPa. Lines passing through the data points are the linear fit to the data. (b) Pressure evolution of FWHM of Raman modes.

with changes in the slope around 8.8 GPa. XRD studies have revealed a structural transition in FNO from trigonal to the monoclinic phase in the range of 8.8–9.3 GPa. Therefore, the change in the slope can be attributed to the above phase transition. The slope values of the mode frequencies with respect to pressure decrease significantly above the transition pressure. The decrease in slopes of the pressure evolution of Raman modes in the monoclinic phase with respect to those in the trigonal phase can be related to the decrease in compressibility. However, it may be noted that the slopes change by around 50%, whereas the compressibility changes only by 8%; possibly, other factors, such as a change in physical properties along with the structure, are responsible. The Nb–O_6 octahedral breathing mode ν_7 shows the maximum change in the frequency with pressure. It can be related to the large distortion of Nb−O_6 octahedra with pressure (Fig. 3). The Fe−O_6 octahedra show a gradual decrease in their distortion until the transition pressure. Therefore, as we discussed earlier, the structural transition can also be viewed as to be driven by increased distortion in the Nb−O_6 octahedra, which becomes more ordered in the monoclinic phase. Interestingly, the FWHM of ν_1', ν_2', and ν_3 shows a minimum at 8.8 GPa [see Fig. 5(b)]. The FWHM of ν_1 keeps on decreasing up to the highest pressure studied. The width of other modes keeps broadening with pressure. The FWHM of a Raman mode is associated with the lifetime of the phonon mode. The anharmonic phonon–phonon scattering events increase the FWHM and, therefore, decrease the lifetime. Therefore, decrease in FWHM of the Raman mode indicates a decrease in anharmonic phonon interactions. Application of pressure gradually induces a strain in the lattice, which is supposed to reduce the lifetime of phonons. A minimum in phonon-mode FWHM can indicate a possibility toward a strong phonon–electron interaction, which causes a decrease in the lifetime of phonons after an electronic phase transition.[9,46–48] To look into the Raman-scattering events, we calculated the normalized intensity of the Raman modes. We have carried out the vector normalization followed by Gautam *et al.*[49] In the vector normalization, first of all, the "norm" of the spectrum is calculated. Then, to obtain the normalized Raman spectrum, each of the Raman intensities corresponding to a wavenumber is divided by the "norm" of that spectrum. Ideally, the intensity of the Raman modes is supposed to reduce under pressure due to the induced lattice strain. Interestingly, the normalized integrated intensity of the ν_1', ν_2'', and ν_3 Raman modes shows a maximum at about 8 GPa as shown in Fig. 6. The sharpening of these modes along with the increase in the intensity up to about 8 GPa shows reduction in anharmonic phonon scattering events. These results indicate an electronic transition along with the structural transition as described earlier. At this point, it is important to point out that low temperature studies on FNO have revealed an antiferromagnetic transition at about 95 K followed by a structural transition to a monoclinic phase at about 85 K, which remained in an antiferromagnetic state.[14] Low temperature Raman spectroscopic studies on a sister material $Mn_4Nb_2O_9$ do not show any anomalous behavior in its Raman modes across its antiferromagnetic transition temperature of about 110–130 K.[40]

Let us now look into the behavior of the electronic Raman-scattering response by analyzing the response of LFE and HFE contributions with pressure. The LFE scattering rate showing an almost exponential decrease with the maximum drop up to about 8 GPa [Fig. 7(a)]. The XRD analysis confirms the gradual decrease of the distortion of both the FeO_6 octahedra with increasing pressure in the trigonal phase. A decrease in the LFE scattering rate also indicates the sharp reduction of lattice distortion with

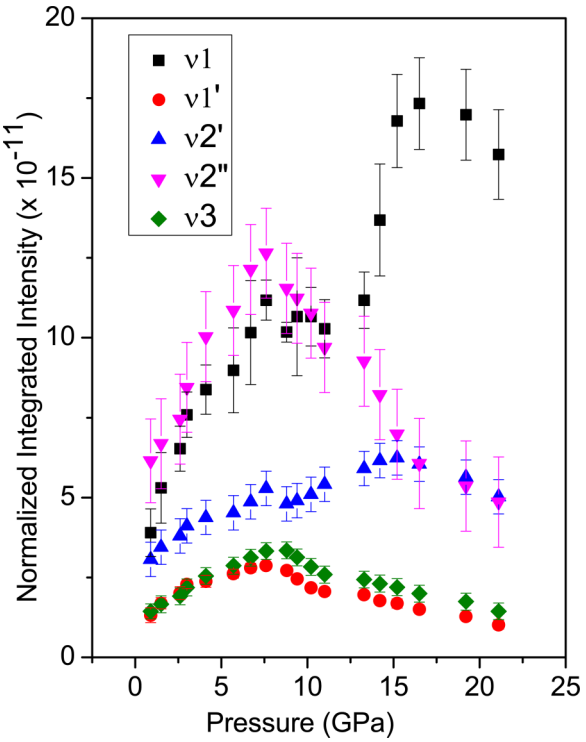

FIG. 6. Pressure dependence of the normalized integrated intensity of Raman modes. The ν_1', ν_2'', and ν_3 Raman mode intensities showing a maximum at about 8 GPa pressure. The intensity of the modes, ν_1 and ν_2', increasing with pressure with an anomaly at about 8 GPa.

increasing pressure. Therefore, one can assume that the Jahn–Teller distortion of the octahedra decreases gradually, which consequently increases charge delocalization, leading to a possibility of an insulator to metal transition. On the other hand, the peak value of the high-frequency inelastic electronic contribution hardens up to about 8 GPa, and its intensity decreases by an order of magnitude up to about 14 GPa [Figs. 7(b) and 7(c)]. The HFE contribution is suggested to be associated with the local polaron formations due to lattice distortions.[29] The peak value of the HFE contribution is attributed to the ionization energy of the polarons. The maximum peak value of the HFE contribution is approximately equal to about 91 meV, which is much smaller than the polaron formation energy[50] as well as estimates obtained for the band structure due to Jahn–Teller splitting[51] and also estimates obtained for perovskite manganese oxides.[29] In addition, reduction of the HFE intensity shows that there is a decrease in scattering cross section of phonons with excited electrons, leading to a decrease in the density of states at the Fermi energy.[26] Several other strongly correlated systems, those undergo paramagnetic insulator phase to ferro-/antiferro-magnetic metallic transition at low temperatures, have shown hardening of the HFE contribution in both intensity as well as its peak position and also a decrease in the LFE contribution up to the transition temperature.[29,52,53] In a high-pressure Raman study on a manganese oxide perovskite system, both the LFE and HFE contributions did not show the expected behavior of insulator to metal transition, and the authors predicted a new un-characterized phase at high pressures.[28] Therefore, considering our LFE and HFE contributions with pressure, we can exclude an insulator to metal transition in our system.

Though across the low temperature phase transition with the distortion index of Nb–O_6 octahedra remaining almost the same (decreases by only about 3%), both the Fe−O_6 octahedra also show a significant increase in the distortion index.[14] In the present work, the distortion index of both the Fe−O_6 octahedra reduces significantly up to the transition pressure, but after the transition pressure, the distortion shows a sudden increase (for Fe1−O_6 octahedra, it is 31%, and for Fe2−O_6 octahedra, it is about 18%). The evidence of the increasing distortion index of both the Fe−O_6 octahedra indicates a JT distortion in the monoclinic phase, which might be responsible for the emergence of a magnetic state. However, it is difficult for us to comment on the exact nature of the magnetic transition in the absence of any magnetization measurements at such high pressure. We can only speculate that if the sample attains a magnetic state, the magnetic nature of this high-pressure monoclinic phase will be similar to that observed in the case of a low temperature monoclinic phase, which is shown to be antiferromagnetic.

In a low temperature study on FNO, Maignan and Martin[1] observed a large peak in the dielectric constant as well as large polarization current (which flipped its sign with reversal of electric field) just below the antiferromagnetic transition temperature. They attributed these observations to the large magnetoelectric effect of FNO in its antiferromagnetic state. It is well known that the normalized Raman mode intensity also depends on the polarization of that particular mode. Therefore, we expect that a change in ferroelectric polarization in the sample may show up in the behavior of the normalized Raman mode intensity. In Fig. 6, we have plotted the pressure evolution of the normalized integrated intensity of ν_1, ν_1', ν_2', ν_2'', and ν_3 modes. The ν_1', ν_2'', and ν_3 modes show a maximum in the intensity around 8 GPa, which also show a minimum in their FWHM at the same pressure range. The ν_1 and ν_2' mode intensities are found to keep increasing up to the highest pressure value with an anomaly at about 15 GPa. The increase in the normalized integrated intensity of all the above modes with pressure may be attributed to a large change in polarization of the sample. Earlier, we have discussed about development of local microscopic order in the sample as a minor monoclinic phase above 0.9 GPa driven by the Nb–O_6 octahedra distortion. This most probably is induced by a gradient in the lattice strain and creates local phases with ferroelectric order. With pressure, the change in local polarization is reflected in the increase of the Raman mode intensity. Similar strain induced nanoscale topological structures with distinct ferroelectric phase have been observed by Yudin *et al.*[54]

From our high-pressure XRD study, we speculate a magnetic transition along with the structural transition about 8 GPa pressure. There may be a possibility that the change in the magnetic structure may induce the anomalies seen in the pressure behavior of the Raman modes due to spin–phonon interactions. However, the effect on Raman mode intensity across any magnetic phase transition in the absence of any applied magnetic field has not been

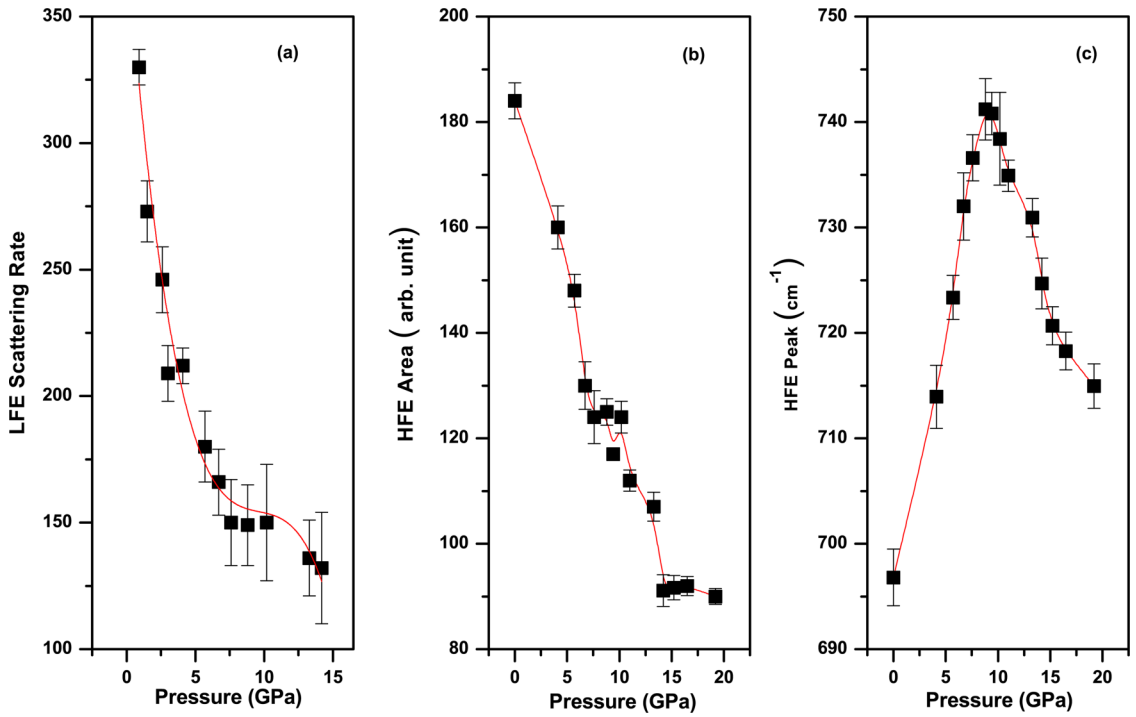

FIG. 7. (a) Diffusive carrier scattering rate of the low-frequency electronic contribution (LFE) to the Raman spectra at different pressures. (b) Normalized integrated intensity and the (c) peak frequency of the high-frequency electronic contribution (HFE) to the Raman spectra at different pressures.

reported to the best of our knowledge. It has been observed that a very high magnetic field is required to produce any significant change across the magnetic transition in the Raman mode intensity.[55–58] Since we have excluded any insulator to metal transition in FNO at high pressure, one can also assume that the spin induced large change in polarization may give rise to the interesting behavior of LFE and HFE contributions to the Raman spectra. To conclude that the high-pressure monoclinic phase of FNO exhibits a magnetoelectric behavior, one needs to carry out dielectric, pyroelectric, domain switching, magnetization, magnetic susceptibility measurements, etc.[59] However, these experiments are highly challenging under high-pressure environment and beyond the scope of the present study. Therefore, we can only speculate about a possible multiferroic state in the high-pressure monoclinic phase of FNO.

IV. CONCLUSION

The phase transitions in $Fe_4Nb_2O_9$ are investigated in detail at high pressures by means of x-ray diffraction and Raman spectroscopy measurements. Our XRD results show a structural transition from ambient trigonal $P\text{-}3c1$ to monoclinic $C2/c$ at high pressures. There is a large increase in both the quadratic elongation and the distortion index of Nb–O_6 octahedra up to about 8.8 GPa followed by a sudden decrease in the monoclinic phase. In contrast, both the Fe−O_6 octahedra become more ordered with pressure in the trigonal phase. All the prominent Raman modes show a slope change in their linear behavior at the structural transition pressure. Some of the Raman modes show a minimum in their FWHM at the same pressure, indicating an electronic transition. A decrease in the diffusive scattering rate is observed in the LFE contribution to the Raman spectra, indicating charge delocalization. However, an observed decrease in the amplitude of the HFE contribution and its peak frequency excludes an insulator to metal transition. The intensity of the Raman modes showing minimum in their FWHM shows a large peak at about 8.8 GPa, indicating a large change in ferroelectric polarization in FNO at the phase transition pressure. Our study shows that the sample may transform to a possible multiferroic state in its high-pressure monoclinic phase.

SUPPLEMENTARY MATERIAL

See the supplementary material that contains additional figures in support of the discussion in the paper.

ACKNOWLEDGMENTS

The authors gratefully acknowledge the financial support from the Department of Science and Technology, Government of India to visit the XPRESS beamline in the ELETTRA Synchrotron light source under the Indo-Italian Executive Programme of Scientific and Technological Cooperation. M.S. gratefully acknowledges the CSIR, Government of India for the financial support to carry out Ph.D. work.

AUTHOR DECLARATIONS

Conflict of Interest

The authors have no conflicts to disclose.

Author Contributions

All authors contributed equally to this work.

DATA AVAILABILITY

The data that support the findings of this study are available within the article and its supplementary material.

REFERENCES

[1]A. Maignan and C. Martin, Phys. Rev. B **97**, 161106 (2018).
[2]Y. Cao, M. Xiang, Z. Feng, B. Kang, J. Zhang, N. Guiblin, W. Ren, B. Dkhil, and S. Cao, RSC Adv. **7**, 13846 (2017).
[3]G. Deng, Y. Yu, Y. Cao, Z. Feng, W. Ren, S. Cao, A. J. Studer, J. R. Hester, Y. Kareri, C. Ulrich, and C. McIntyre, J. Phys.: Condens. Matter **31**, 235801 (2019).
[4]L. Yin, Y. Zou, J. Yang, J. Dai, W. Song, X. Zhu, and Y. Sun, Appl. Phys. Lett. **109**, 032905 (2016).
[5]J.-P. Rivera, Eur. Phys. J. B **71**, 299 (2009).
[6]H. Schmid, Ferroelectrics **162**, 317 (1994).
[7]A. Agyei and J. L. Birman, J. Phys.: Condens. Matter **2**, 3007 (1990).
[8]Y. Tokunaga, N. Furukawa, H. Sakai, Y. Taguchi, T.-H. Arima, and Y. Tokura, Nat. Mater. **8**, 558 (2009).
[9]R. Jana, P. Saha, V. Pareek, A. Basu, S. Kapri, S. Bhattacharyya, and G. D. Mukherjee, Sci. Rep. **6**, 31610 (2016).
[10]N. D. Khanh, N. Abe, S. Kimura, Y. Tokunaga, and T. Arima, Phys. Rev. B **96**, 094434 (2017).
[11]Y. Fang, Y. Song, W. Zhou, R. Zhao, R. Tang, H. Yang, L. Lv, S. Yang, D. Wang, and Y. Du, Sci. Rep. **4**, 3860 (2014).
[12]S. N. Panja, L. Harnagea, J. Kumar, P. K. Mukharjee, R. Nath, A. K. Nigam, and S. Nair, Phys. Rev. B **98**, 024410 (2018).
[13]Y. M. Xie, C. S. Lin, H. Zhang, and W. D. Cheng, AIP Adv. **6**, 045006 (2016).
[14]R. Jana, D. Sheptyakov, X. Ma, J. A. Alonso, M. Pi, A. Muñoz, Z. Liu, L. Zhao, N. Su, S. Jin *et al.*, Phys. Rev. B **100**, 094109 (2019).
[15]L. Ding, Y. Wu, M. Lee, E. S. Choi, R. Sinclair, H. Zhou, B. C. Chakoumakos, and H. Cao, "Successive dielectric anomalies and magnetoelectric coupling in honeycomb $Fe_4Nb_2O_9$," arXiv:2003.01029 (2020).
[16]N. Khanh, N. Abe, H. Sagayama, A. Nakao, T. Hanashima, R. Kiyanagi, Y. Tokunaga, and T. Arima, Phys. Rev. B **93**, 075117 (2016).
[17]B. Liu, Y. Fang, Z. Han, S. Yan, W. Zhou, B. Qian, D. Wang, and Y. Du, Mater. Lett. **164**, 425 (2016).
[18]E. Bertaut, L. Corliss, F. Forrat, R. Aleonard, and R. Pauthenet, J. Phys. Chem. Solids **21**, 234 (1961).
[19]Y. Fang, W. Zhou, S. Yan, R. Bai, Z. Qian, Q. Xu, D. Wang, and Y. Du, J. Appl. Phys. **117**, 17B712 (2015).
[20]A. Maignan and C. Martin, Phys. Rev. Mater. **2**, 091401 (2018).
[21]N. Lee, D. G. Oh, S. Choi, J. Y. Moon, J. H. Kim, H. J. Shin, H. Y. Choi, K. Son, M. J. Gutmann, G. Kim *et al.*, "Highly nonlinear magnetoelectric effect in antiferromagnetic $Co_4Ta_2O_9$ single crystals," arXiv:1905.00591 (2019).
[22]M. Fiebig, J. Phys. D: Appl. Phys. **38**, R123 (2005).
[23]L. Ding, C. Colin, C. Darie, J. Robert, F. Gay, and P. Bordet, Phys. Rev. B **93**, 064423 (2016).
[24]N. Khanh, N. Abe, K. Matsuura, H. Sagayama, Y. Tokunaga, and T. Arima, Appl. Phys. Lett. **114**, 102905 (2019).
[25]H. Huang, Z. Chen, R.P. Wang et al., Nat. Commun. **8**, 15929 (2017).
[26]R. Gupta, A. Sood, R. Mahesh, and C. Rao, Phys. Rev. B **54**, 14899 (1996).
[27]D. Marrocchelli, P. Postorino, D. Di Castro, E. Arcangeletti, P. Dore, M. C. Guidi, S. Ray, and D. Sarma, Phys. Rev. B **76**, 172405 (2007).
[28]A. Congeduti, P. Postorino, E. Caramagno, M. Nardone, A. Kumar, and D. Sarma, Phys. Rev. Lett. **86**, 1251 (2001).
[29]S. Yoon, H. L. Liu, G. Schollerer, S. L. Cooper, P. Han, D. Payne, S.-W. Cheong, and Z. Fisk, Phys. Rev. B **58**, 2795 (1998).
[30]T. Katsufuji and Y. Tokura, Phys. Rev. B **49**, 4372 (1994).
[31]A. Dewaele, M. Torrent, P. Loubeyre, and M. Mezouar, Phys. Rev. B **78**, 104102 (2008).
[32]A. Hammersley, S. Svensson, M. Hanfland, A. Fitch, and D. Hausermann, Int. J. High Pressure Res. **14**, 235 (1996).
[33]R. Shirley, "The Crysfire system for automatic powder indexing" (The Lattice Press, Guildford, England, 2002).
[34]J. Laugier and B. Bochu, CHEKCELL is a modified version of CELREF for analysing the solutions given by the CRYSFIRE program, Developped at Laboratoire des Matériaux et du Génie Physique, Ecole Nationale Supérieure de Physique de Grenoble (INPG), Domaine Universitaire BP 46, 38402 Saint Martin d'Hères, France.
[35]B. H. Toby, J. Appl. Crystallogr. **34**, 210 (2001).
[36]H. Mao, J.-A. Xu, and P. Bell, J. Geophys. Res. Solid Earth **91**, 4673, https://doi.org/10.1029/JB091iB05p04673 (1986).
[37]W. Kraus and G. Nolze, J. Appl. Crystallogr. **29**, 301 (1996).
[38]W. Kraus and G. Nolze, "PowderCell 2.3 — powder pattern calculation from single crystal data and refinement of experimental curves" (Federal Institute for Materials Research and Testing, Berlin, 2000).
[39]R. J. Angel, M. Alvaro, and J. Gonzalez-Platas, Z. Kristallogr. Cryst. Mater. **229**, 405 (2014).
[40]C. Chen, Q. Wang, H. Chen, Y. Cao, and Z. Li, AIP Adv. **9**, 125124 (2019).
[41]J. Rodrigues, D. Bezerra, R. Costa, P. Pizani, and A. Hernandes, J. Raman Spectrosc. **48**, 1243 (2017).
[42]J. Rodrigues, D. Bezerra, and A. Hernandes, Ceram. Int. **43**, 14015 (2017).
[43]J. Rodrigues, P. Castro, P. Pizani, W. Correr, and A. Hernandes, Ceram. Int. **42**, 18087 (2016).
[44]C. Ulrich, G. Khaliullin, M. Guennou, H. Roth, T. Lorenz, and B. Keimer, Phys. Rev. Lett. **115**, 156403 (2015).
[45]M. N. Iliev and M. V. Abrashev, J. Raman Spectrosc. **32**, 805 (2001).
[46]S. N. Gupta, A. Sing, K. Pal, B. Chakraborti, D. V. S. Muthu, U. V. Waghmare, and A. K. Sood, Phys. Rev. B **96**, 094104 (2017).
[47]P. Saha, B. Ghosh, R. Jana, and G. Dev Mukherjee, J. Appl. Phys. **123**, 204306 (2018).
[48]A. Bera, K. Pal, D. Muthu, S. Sen, P. Guptasarma, U. V. Waghmare, and A. Sood, Phys. Rev. Lett. **110**, 107401 (2013).
[49]R. Gautam, S. Vanga, F. Ariese, and S. Umapathy, EPJ Tech. Instrum. **2**, 8 (2015).
[50]M. Jaime, M. Salamon, M. Rubinstein, R. Treece, J. Horwitz, and D. Chrisey, Phys. Rev. B **54**, 11914 (1996).
[51]S. Satpathy, Z. S. Popovic, and F. R. Vukajlovic, Phys. Rev. Lett. **76**, 960 (1996).
[52]S. Billinge, R. DiFrancesco, G. Kwei, J. Neumeier, and J. Thompson, Phys. Rev. Lett. **77**, 715 (1996).
[53]C. Girardot, J. Kreisel, S. Pignard, N. Caillault, and F. Weiss, Phys. Rev. B **78**, 104101 (2008).
[54]P. Yudin, J. Duchon, O. Pacherova, M. Klementova, T. Kocourek, A. Dejneka, and M. Tyunina, Phys. Rev. Res. **3**, 033213 (2021).
[55]R. Sooryakumar and M. V. Klein, Phys. Rev. B **23**, 3213 (1981).
[56]J. Ji, A. Zhang, J. Fan, Y. Li, X. Wang, J. Zhang, E. W. Plummer, and Q. Zhang, Proc. Natl. Acad. Sci. U.S.A. **113**, 2349 (2016).
[57]A. McCreary, T. T. Mai, F. G. Utermohlen et al., Nat. Commun. **11**, 3879 (2020).
[58]J.-M. Li, A. C. H. Huan, L. Wang, Y.-W. Du, and D. Feng, Phys. Rev. B **61**, 6876 (2000).
[59]X. Liu, W. Song, M. Wu, Y. Yang, Y. Yang, P. Lu, Y. Tian, Y. Sun, J. Lu, J. Wang, D. Yan, Y. Shi, N. X. Sun, Y. Sun, P. Gao, K. Shen, G. Chai, S. Kou, C.-W. Nan, and J. Zhang, Nat. Commun. **12**, 5453 (2021).